JOM, Vol. 66, No. 10, 2014
DOI: 10.1007/s11837-014-1133-6

Composition Dependence of Phase Stability, Deformation Mechanisms, and Mechanical Properties of the CoCrFeMnNi High-Entropy Alloy System

C. C. TASAN,[1,3] Y. DENG,[1] K. G. PRADEEP,[1,2] M. J. YAO,[1] H. SPRINGER,[1] and D. RAABE[1]

1.—Max-Planck Institut für Eisenforschung, 40237 Düsseldorf, Germany. 2.—Materials Chemistry, RWTH Aachen University, 52074 Aachen, Germany. 3.—e-mail: c.tasan@mpie.de

The proposal of configurational entropy maximization to produce massive solid-solution (SS)-strengthened, single-phase high-entropy alloy (HEA) systems has gained much scientific interest. Although most of this interest focuses on the basic role of configurational entropy in SS formability, setting future research directions also requires the overall property benefits of massive SS strengthening to be carefully investigated. To this end, taking the most promising CoCrFeMnNi HEA system as the starting point, we investigate SS formability, deformation mechanisms, and the achievable mechanical property ranges of different compositions and microstructural states. A comparative assessment of the results with respect to room temperature behavior of binary Fe-Mn alloys reveals only limited benefits of massive SS formation. Nevertheless, the results also clarify that the compositional requirements in this alloy system to stabilize the face-centered cubic (fcc) SS are sufficiently relaxed to allow considering nonequiatomic compositions and exploring improved strength–ductility combinations at reduced alloying costs.

INTRODUCTION

High-entropy alloys (HEAs) are newly developed, multicomponent alloys wherein the configurational entropy (CE) is higher than the fusion entropy of most common metals.[1] These alloys draw increasing scientific interest, especially regarding the fundamental aspects of massive solid-solution (SS) phases and the basic role of CE therein.[2–5] These efforts are well motivated, as the HEA concept was originally based on CE maximization (i.e., by increasing the number of equiatomically proportioned alloying elements). However, this strategy has led so far to only a few successful single-phase alloys,[6–8] and the role of CE in these successful cases is being debated.[9,10] Instead, most of the investigated alloys pertaining to this class develop complex, multiphase microstructures and low tensile ductility, providing limited prospects for future applications.[11] Even for the present success stories such as $Co_{20}Cr_{20}Fe_{20}Mn_{20}Ni_{20}$, the most promising HEA with a highly stable and ductile single-phase SS,[6,9,12–19] the specific composition tolerance window, the weak high-temperature behavior, and the expensive alloying (e.g., Ni) are still pending challenges. Considering that the overall applicability of a new material class is strongly linked to the versatility of the properties it can deliver in exchange for the practical and economical complexities created by its bulk processing,* the above-mentioned difficulties and uncertainties call for a critical assessment of the versatility versus complexity balance in HEA. The main aim of this work is to provide such an analysis as well as new perspectives to improve on the aforementioned limiting aspects. Thus in what follows, taking the reported weak CE dependence of the $Co_{20}Cr_{20}Fe_{20}Mn_{20}Ni_{20}$ alloy as the starting point, we investigate alloys of different compositions and/or different number of alloying elements to assess compositional effects on single-phase SS formation, deformation mechanisms, and resulting mechanical properties. In other words, the possibilities of

*For example dual-phase steels[20–22] or Al7000 alloys[23] can provide a wide spectrum of properties with plain and commercially feasible thermomechanical treatments and inexpensive alloying.

(Published online September 16, 2014)

expanding the limits of the property space of this alloy system will be investigated at the expense of decreasing configurational entropy.

METHODOLOGY

In this work, a combinatorial approach is employed for rapid trend screening of metallurgically melted nonequiatomic CoCrFeMnNi and CoCrFeMn alloys.[24] The produced compositions span over wide ranges for both systems: $Fe_{(64-x)}Mn_x$-$Ni_{27.7\pm1.3}Co_{5.6\pm0.3}Cr_{2.3\pm0.1}$ (x = 21/24/27/34/38) and $Fe_{(80-y)}Mn_yCo_{10\pm1}Cr_{10\pm1}$ (y = 31/35/42, 45) (at.% throughout this work). These two systems were selected as they enable the investigation of the influence of several parameters (e.g., configurational entropy, Ni content, and stacking fault energy) on the overall properties. To this end, it is of specific importance to assess the limits of single SS formability. In fact, the latter system allows investigating the transition from a single phase to a multiphase microstructure. In the current report, however, the focus is placed on one nonequiatomic alloy from each alloy class, i.e., $Fe_{40}Mn_{27}Ni_{26}Co_5Cr_2$ and $Fe_{37}Mn_{45}Co_9Cr_9$, respectively, demonstrating the selected overall characteristics of these two systems. A more comprehensive investigation of the property trends in these systems will be treated elsewhere. To assess the relative contributions of CE, several results are compared with those from the equiatomic $Co_{20}Cr_{20}Fe_{20}Mn_{20}Ni_{20}$ and $Co_{25}Cr_{25}Fe_{25}Mn_{25}$ systems, either from the literature (for the former) or referring to the presented new data in this article (for the latter).

The alloys were melted from pure metals (purity $>$99.9 wt.%) in a vacuum-induction furnace under 400 mbar Ar pressure and subsequently cast into water-cooled copper molds. After each cast, the remaining melt composition in the ingot was adjusted by charging Mn through an air lock. After cooling and cutting into blocks, a small amount of material was kept for the characterization of the as-cast structure, whereas the rest was hot rolled to 50% thickness reduction at 900°C. The rolled sheets were then reheated for homogenization treatment at 1200°C for 2 h in Ar atmosphere and quenched in water. To investigate the influence of cold working on the mechanical properties, some of the hot-rolled sheets were further cold rolled to 64% engineering thickness reduction. Cross rolling was not applied.

The resulting microstructures were investigated in the as-cast, homogenized, and cold-rolled conditions using various tools and techniques. X-ray diffraction (XRD) measurements were carried out on specimens mounted on a Huber-2 goniometer (Huber Diffraktionstechnik GmbH & Co., KG Rimsting, Germany) and exposed to CoKα radiation (λ = 1.79 Å). The Metero0D detector swept a 2θ range from 0° to 120° with a step size of $\Delta 2\theta$ = 0.05°. Secondary electron (SE) and backscattered electron (BSE) imaging and electron backscatter diffraction (EBSD) analyses were conducted two field-emission-gun scanning electron microscopes, a JEOL 6500F (JEOL Ltd., Tokyo, Japan) and a dual-beam Zeiss-crossbeam XB1560 (Carl Zeiss, Oberkochen, Germany), both equipped with TSL OIM EBSD systems (EDAX Inc., Mahwah, NJ). Grain sizes are determined from EBSD measurements. The deformation and damage mechanisms were also investigated in the latter microscope, employing the electron channelling contrast imaging (ECCI) technique.[25]

Although the overall chemical composition was confirmed by inductively coupled plasma and optical emission spectrometry and infrared absorption measurements, such high-Mn alloys are susceptible to segregation. Thus, chemical homogeneity was studied at the crystal scale using energy-dispersive X-ray spectroscopy (EDX) and atomic scale using a LEAP 3000× HR local electrode atom-probe tomography (APT) setup (Cameca Inc., Gennevilliers, France), although only the latter is shown here. APT specimens were target prepared from EBSD determined grains using a FEI Helios Nanolab 600i dual-beam focused ion beam (FIB) device as described in Ref. [26]

To investigate the mechanical performance of the two alloy systems, tensile tests were carried out employing a miniaturized deformation stage (Kammrath-Weiss GmbH, Dortmund, Germany) and Aramis digital image correlation (DIC) system (GOM GmbH, Braunschweig, Germany). For the follow-up investigation of deformation mechanisms, the samples were metallographically prepared to a colloidal silica finish and investigated at various DIC-determined strain levels using the microscopy techniques described above.

RESULTS

As reported elsewhere, the equiatomic $Co_{20}Cr_{20}$-$Fe_{20}Mn_{20}Ni_{20}$ alloy presents a stable, highly ductile face-centered cubic (fcc) phase.[6,12] The microstructure characterization of the nonequiatomic $Fe_{40}Mn_{27}Ni_{26}Co_5Cr_2$ alloy at different processing states is shown in Fig. 1. The as-cast and homogenized microstructures are shown by EBSD-based phase maps in Fig. 1a and by XRD analysis in Fig. 1b. Both EBSD and XRD analyses carried out on the nonequiatomic $Fe_{40}Mn_{27}Ni_{26}Co_5Cr_2$ system reveal no phase separation and have a stable microstructure consisting fully of fcc grains. The black particles observed in Fig. 1a_2 are indexed as manganese oxide particles, which are challenging to avoid in the processing of high-Mn alloys. The average grain size (GS) is 45 μm. Even low-Mn steels are known to be susceptible to Mn segregation and associated microstructural banding issues;[27] thus, the chemical homogeneities of the alloy are confirmed at the mesoscale by energy-dispersive spectroscopy (EDS)[10] and at the atomic scale by APT (Fig. 1c). The corresponding APT tip lift-out locations are shown in the EBSD maps presented in

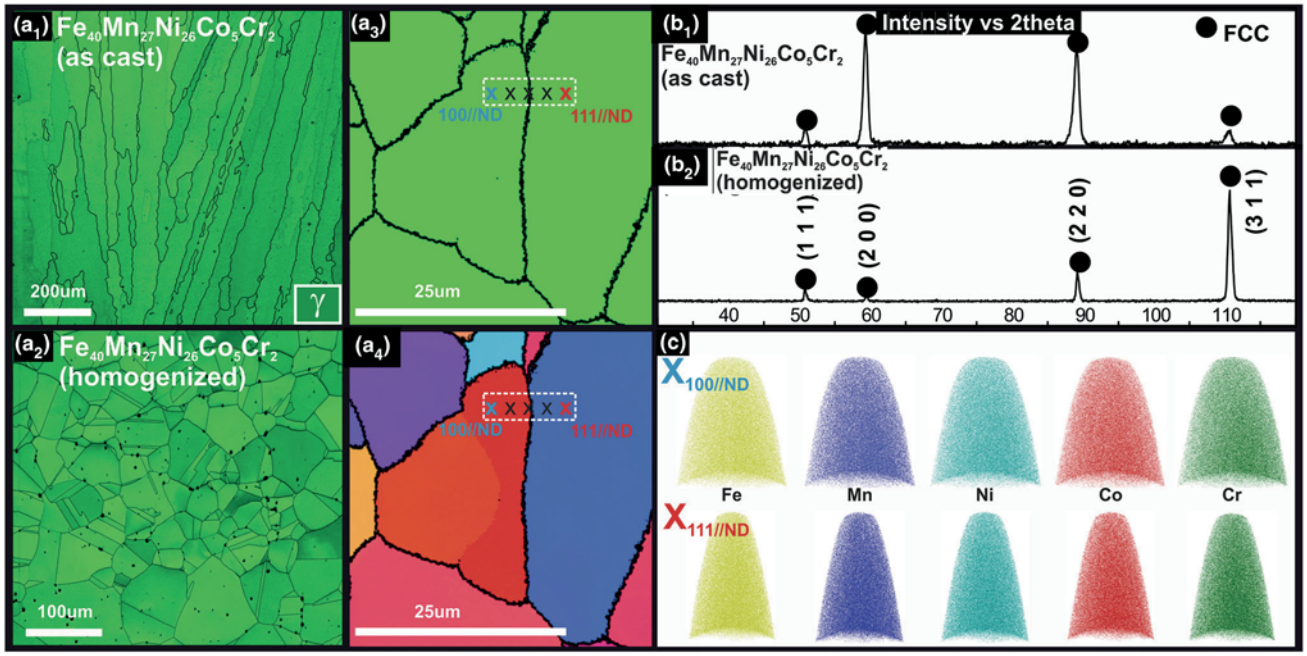

Fig. 1. (a) EBSD- and (b) XRD-based characterization of the nonequiatomic $Fe_{40}Mn_{27}Ni_{26}Co_5Cr_2$ alloy in the (b_1) as-cast and (b_2) homogenized states. (c) APT analysis of tips lifted from the homogenized microstructure from the grains shown in (a_3).

Fig. 1a_3–a_4. Thus, this alloy develops a microstructure that consists of a single fcc phase at all processing states, i.e., including the hot rolled and cold rolled states, the images of which are not shown here.

While the five-component, equiatomic $Co_{20}Cr_{20}Fe_{20}Mn_{20}Ni_{20}$ and nonequiatomic $Fe_{40}Mn_{27}Ni_{26}Co_5Cr_2$ alloys show a stable microstructure consisting of a single fcc phase, the microstructure characterization of the four-component equiatomic $Co_{25}Cr_{25}Fe_{25}Mn_{25}$ alloy reveals a contrasting picture. The optical micrographs of the as-cast microstructure presented in Fig. 2a_1 reveal zones of sharply varying morphology, e.g., from equiaxed to lamellar grains, and the corresponding XRD profile shows that a complex, multiphase microstructure develops after solidification (Fig. 2b), as also reported by others.[13] Due to the development of this multiphase microstructure, this alloy is not investigated further. In contrast, the four-component, nonequiatomic $Fe_{37}Mn_{45}Co_9Cr_9$ alloy has more common features to the aforementioned five-component CoCrFeMnNi alloys, as will be presented next.

Light microscope images of the as-cast $Fe_{37}Mn_{45}Co_9Cr_9$ alloy microstructure consists of typical columnar solidification grain morphology, with only one single apparent phase (Fig. 2a_2), while the XRD profiles reveal dominant fcc peaks, as well as the presence of a single (very weak) hexagonal close-packed (hcp) phase peak (Fig. 2b). Nevertheless, EBSD measurements of the as-cast state taken at two different spatial resolutions show only fcc phase (Fig. 3a). After the homogenization treatment, both the XRD (Fig. 2b) and EBSD measurements (Fig. 3b) reveal the presence of a single fcc phase with an average GS of 90 μm. These observations suggest that the four-component, nonequiatomic $Fe_{37}Mn_{45}Co_9Cr_9$ alloy develops microstructures that consist of a dominant fcc phase for the investigated processing states. In the as-cast state, light microscopy, EBSD and hardness** measurements do not capture the presence or influence of the small amount of hcp phase observed by XRD measurements. This suggests that the hcp phase is dispersed in few widely spaced locations in the microstructure where solidification-induced heterogeneity is more enhanced. After homogenization, it is easily removed and a full fcc microstructure with equiaxed grains is developed.

Examples of lower-bound stress–strain response of the five-component, nonequiatomic $Fe_{40}Mn_{27}Ni_{26}Co_5Cr_2$ (GS of 45 μm) and four-component, nonequiatomic $Fe_{37}Mn_{45}Co_9Cr_9$ (GS of 90 μm) alloys are given in Fig. 4a, followed by the characterization of deformation mechanisms (Figs. 5, 6, 7, and 8). These microstructure analyses are carried out at different positions in the fractured sample corresponding to different deformation levels (see, e.g., the strain distribution at the onset of failure for the $Fe_{37}Mn_{45}Co_9Cr_9$ alloy in Fig. 4a). To investigate

**A total of 25 indentation experiments carried out at different processing states reveal an increase in the as-cast Vickers hardness value (under1 kg. load) of 130 ± 3 to 200 ± 10 in the hot-rolled state (during which only partial recrystallization is observed), while the hardness of the homogenized state drops down to the as cast state level at 139 ± 9.

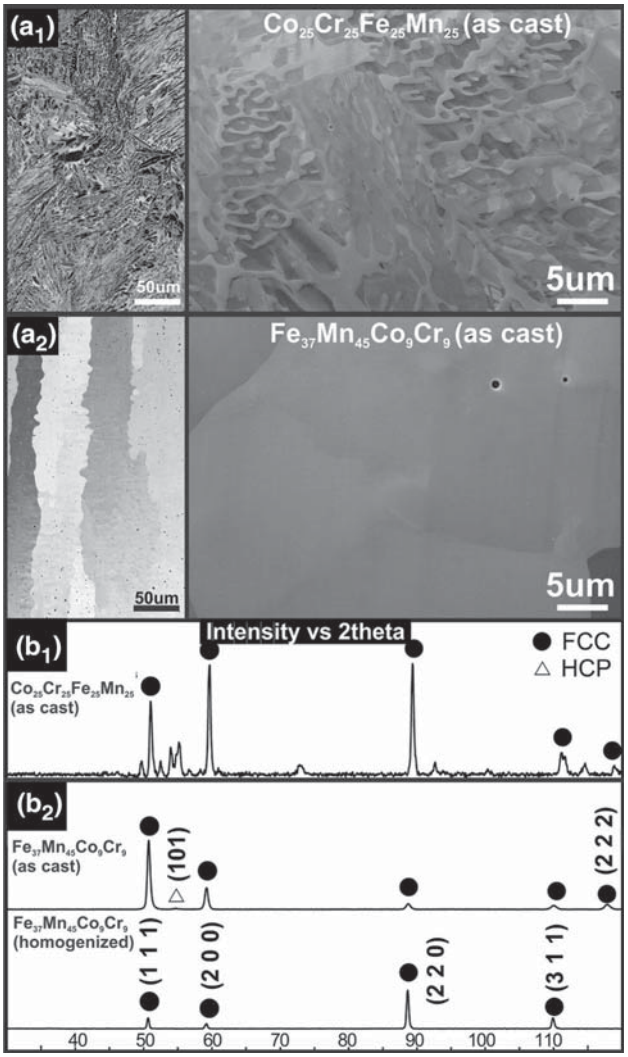

Fig. 2. (a) Light microscopy and (b) XRD-based characterization of the four-component, (b_1) $Co_{25}Cr_{25}Fe_{25}Mn_{25}$ and (b_2) $Fe_{37}Mn_{45}Co_9Cr_9$ alloys (as cast and homogenized).

the influence of prestraining, the stress–strain response and the damage resistance behaviour of the cold rolled state are also provided in Figs. 4 and 8, respectively.

The mechanical behaviors of the homogenized $Fe_{40}Mn_{27}Ni_{26}Co_5Cr_2$ and $Fe_{37}Mn_{45}Co_9Cr_9$ alloys are remarkably similar, except for a ~10% difference in overall ductility. Upon cold rolling the former, a strong (~700%) increase in the yield strength is observed, while almost all uniform ductility is lost. However, a prolonged plastic instability regime is observed upon necking until failure is observed at a strain level of 18%.

The averaged tensile properties of these two alloys are compared with those of (I) binary Fe-Mn alloys (from Refs. 28 and 29) and of (I.I) equiatomic $Co_{20}Cr_{20}Fe_{20}Mn_{20}Ni_{20}$ alloy (from[12]). Considering the fully austenitic microstructures of the alloys investigated in this article and the 1-to-2 equivalency for Mn and Ni contents,[30] the properties of the alloys are plotted next to the fully austenitic Fe-Mn region (with Mn >28%). This comparison reveals that (I) the mechanical properties of all three alloys are comparable with high-Mn binary Fe-Mn alloys (although grain refinement typically leads to improved properties) and (II) all three alloys have comparable mechanical response with respect to each other, although the four-component $Fe_{37}Mn_{45}Co_9Cr_9$ alloy has relatively lower strength and ductility values.

To understand the deformation micromechanisms causing this macroscopic response, first the deformation-induced evolution of the grain boundary misorientation distribution in $Fe_{40}Mn_{27}Ni_{26}Co_5Cr_2$ is presented (Fig. 5). Here, the microstructure maps corresponding to different deformation levels are also provided, as well as the Schmid factor map of the first deformation state.

Three observations can be made based on the maps and chart provided in Fig. 5. First, a comparison of the Schmid factor and the kernel average misorientation map corresponding to 3% local strain reveals that plasticity is triggered at grains with preferable crystallographic orientation (see the blue arrows), even when those grains are relatively smaller than others in dimension. Second, increasing deformation leads to a decrease in the density of high-angle grain boundaries (many of which were originally inherited annealing twin boundaries) and an increase in the density of low-angle boundaries. Third, the increase in low-angle boundary density takes place at a higher rate in smaller grains, as revealed by the maps in Fig. 5.

Next, we focus on surface trace analysis on (prepolished, then deformed) samples (Fig. 6). Here, in Fig. 6a, the overview image is provided, and important aspects are highlighted in cropped images Fig. 6b_1–b_4. At low deformation levels a single slip system is triggered first and the entire crystal undergoes relatively homogeneous slip-based plastic deformation. Typical heterogeneities arise due to slip transition conditions with surrounding grains; i.e., depending on the ease of slip transition, either dislocation pile-up induced roughening (Fig. 6b_1) or activation of other slip systems (Fig. 6b_2) is observed. Also, a variation in the height of the surface steps is clearly observed from the grain interior toward grain boundaries, suggesting that slip is initially triggered in the center of the grains away from the boundaries (Fig. 6b_3). Interestingly, at these same low deformation levels, smaller grains already exhibit activation of multiple slip systems, clearly because of the more constrained strain compatibility conditions with respect to the surrounding crystals (Fig. 6b_4). This observation confirms the higher increase rate of low-angle grain boundaries shown in Fig. 5.

The microstructural deformation mechanisms responsible of the presented stress–strain response are clearly revealed by ECCI (Fig. 7). Here, Fig. 7a_1–a_4 map deformation substructures in the

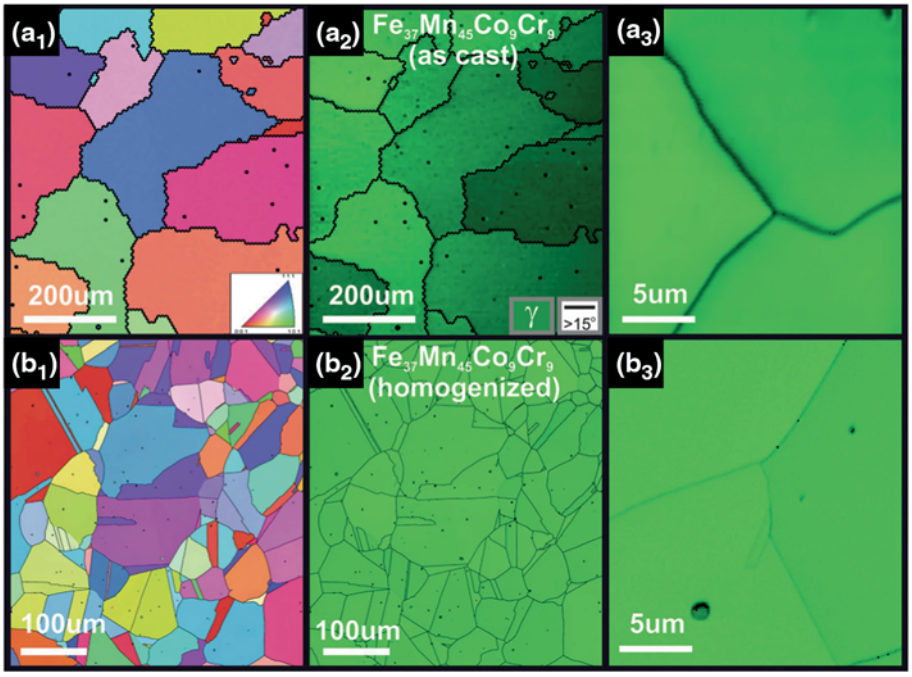

Fig. 3. (a) As-cast and (b) homogenized $Fe_{37}Mn_{45}Co_9Cr_9$ alloy characterized by EBSD based (b_1) inverse pole figure maps, (b_2) phase maps, and (b_3) high resolution phase maps.

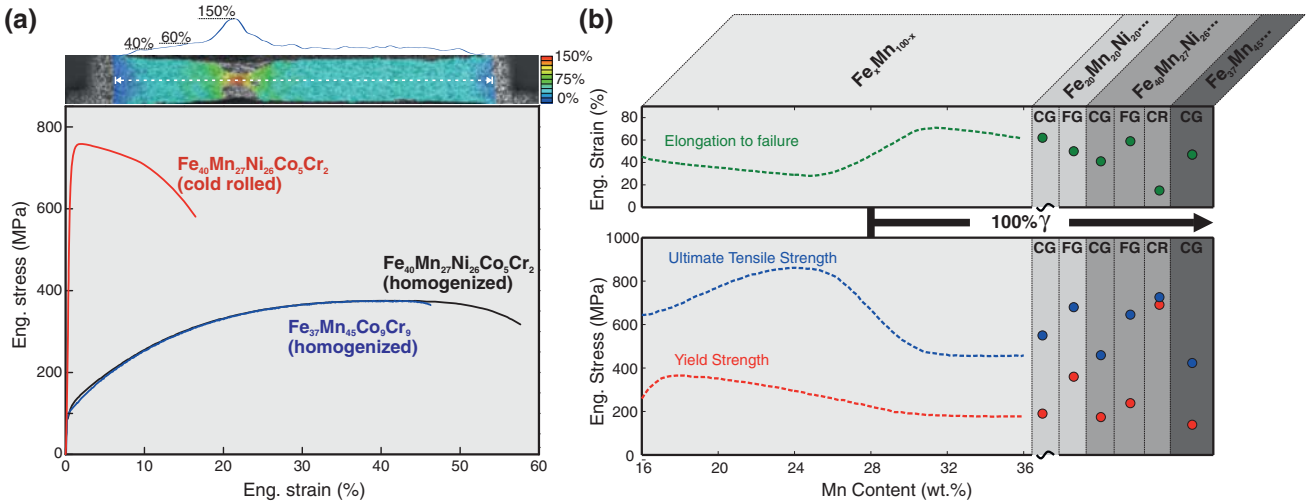

Fig. 4. (a) Example stress–strain curves (lower bound) of the homogenized $Fe_{37}Mn_{45}Co_9Cr_9$ and $Fe_{40}Mn_{27}Ni_{26}Co_5Cr_2$ alloys. The tensile response of the cold rolled $Fe_{40}Mn_{27}Ni_{26}Co_5Cr_2$ alloy is also provided. An example of the DIC-based local strain map showing the strain distribution prior to failure in the $Fe_{40}Mn_{27}Ni_{26}Co_5Cr_2$ alloy. (b) Comparison of the average properties of the investigated alloys to tensile test properties of binary Fe-Mn alloys reproduced from literature[28,29] and to the equiatomic CoCrFeMnNi alloy.[12] Here, CG: coarse grained (i.e., 155 μm for the equiatomic alloy, 45 μm for the five-component alloy, and 90 μm for the four-component alloy), FG: fine grained (i.e., 4.4 μm for the equiatomic alloy and 12 μm for the five-component alloy), CR: cold-rolled, red data points: yield strength, blue data points: ultimate tensile strength, and green data points: elongation to failure.

$Fe_{40}Mn_{27}Ni_{26}Co_5Cr_2$ alloy at ~3%, ~5%, ~10%, and ~30% local strain, and Fig. 7b_1–b_2 in the $Fe_{37}Mn_{45}Co_9Cr_9$ alloy at ~3% and ~10% local strain.

In Fig. 7a_1, piled-up dislocations at an annealing twin are imaged. The dislocations are arrayed on well-defined planes on both sides of the twin as well as inside it (yellow arrows). One of the dislocation pileups (bottom yellow arrow) is enlarged in the inset for a clearer view. These observations are typical at low deformation levels, especially in large grains. In contrast, multiple slip systems are already activated in smaller grains at this loading stage (Fig. 7a_2). Increasing deformation leads to the formation of extended dislocation pileups in many adjacent planes (that correspond to {111} planes, as

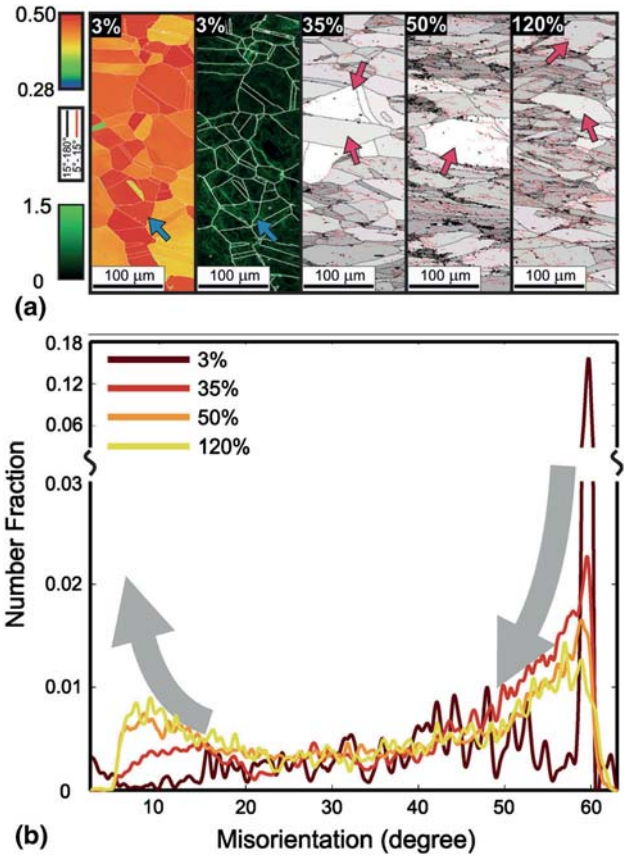

Fig. 5. (a) Deformation-induced evolution of grain boundary misorientation distribution in the $Fe_{40}Mn_{27}Ni_{26}Co_5Cr_2$ alloy, shown together with the grain average image quality maps with boundary overlays, as well as (b) the Schmid factor map of the first deformation stage.

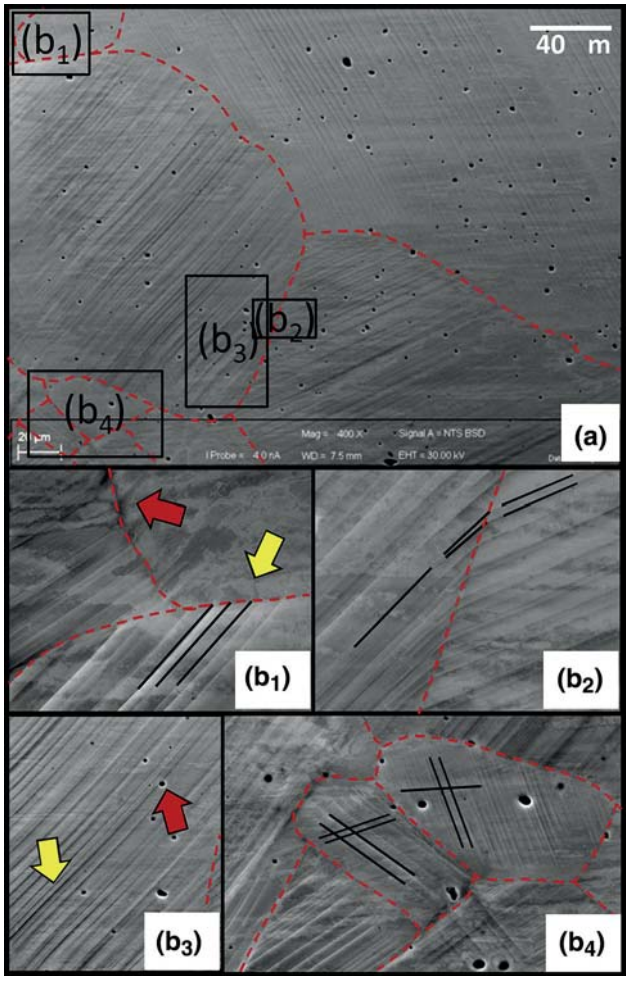

Fig. 6. Surface trace analysis of the $Fe_{40}Mn_{27}Ni_{26}Co_5Cr_2$ alloy during early uniform deformation, providing insight on slip transition (b_1 versus b_2), slip initiation (b_3) and GS effect on slip system activation (b_1 versus b_4).

confirmed by EBSD); see Fig. 7a_3. However, at higher deformation levels, the planarity of dislocation slip is relaxed and indications of nonplanar slip are observed, e.g., dislocation cells (Fig. 7a_4). As expected from the very similar stress–strain response presented in Fig. 4, the $Fe_{37}Mn_{45}Co_9Cr_9$ alloy exhibits the same deformation mechanisms despite the different composition (Fig. 7b_1, b_2). Thus, the ECCI images presented here demonstrate that both nonequiatomic $Fe_{40}Mn_{27}Ni_{26}Co_5Cr_2$ and $Fe_{37}Mn_{45}Co_9Cr_9$ HEAs exhibit planar slip at low deformation levels and wavy slip at high deformation levels.

When focusing on the final stage of deformation, we find that the BSE images of the cross section of the fractured tensile tests samples reveal four main observations regarding the failure mechanisms in the $Fe_{40}Mn_{27}Ni_{26}Co_5Cr_2$ alloy: (I) The microstructure is resistant to deformation-induced microcrack formation (see the large damage densities in Fig. 8a_1–b_1); (II) this resistance is partially due to the nanotwins observed within the localized neck around the cracks (see red and yellow arrows in Fig. 8b_3; (III) the multilayered microstructure morphology formed during rolling (see yellow arrows in Fig. 8b_1, b_2) also contributes to the crack resistance; and (IV) despite significant damage evolution, rather than cup-cone type of failure, the alloy fails via through-thickness shear fracture (see insets in Fig. 8a_1, b_1).

DISCUSSION

For the four alloys considered, CEs and different SS formation criteria from the literature are compared in Table I. It can be observed that a ~23% decrease in the CE from $Co_{20}Cr_{20}Fe_{20}Mn_{20}Ni_{20}$ to $Fe_{40}Mn_{27}Ni_{26}Co_5Cr_2$ alloy does not lead to any change in the stability of the massive SS fcc phase, whereas a decrease of ~20% in the CE from the $Co_{25}Cr_{25}Fe_{25}Mn_{25}$ to the $Fe_{37}Mn_{45}Co_9Cr_9$ alloy even favors the formation of a single-phase SS. These results contribute to previous works from the literature that indicate the indecisive role of the CE criterion alone on the formation of SS alloy.[9–11] It is also interesting to note that although the high CE values of the nonequiatomic alloys allow them to be

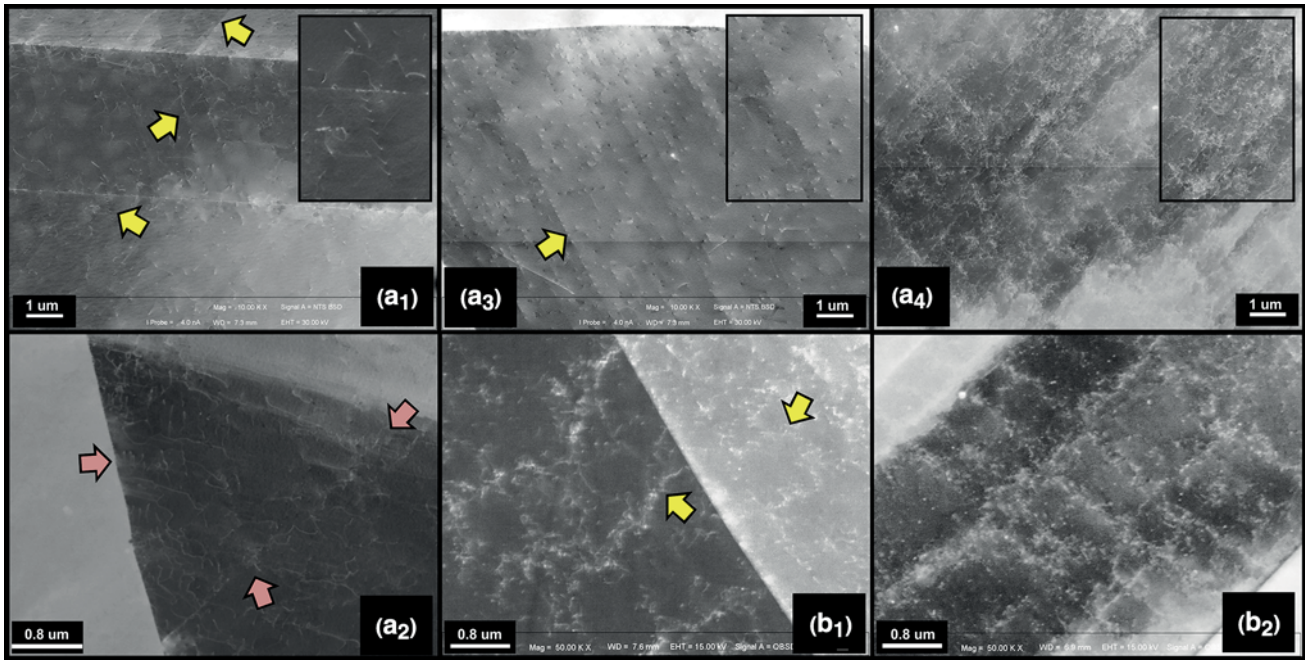

Fig. 7. ECCI based deformation microstructure characterization of (a) $Fe_{40}Mn_{27}Ni_{26}Co_5Cr_2$, and (b) $Fe_{37}Mn_{45}Co_9Cr_9$ alloys at increasing strain levels.

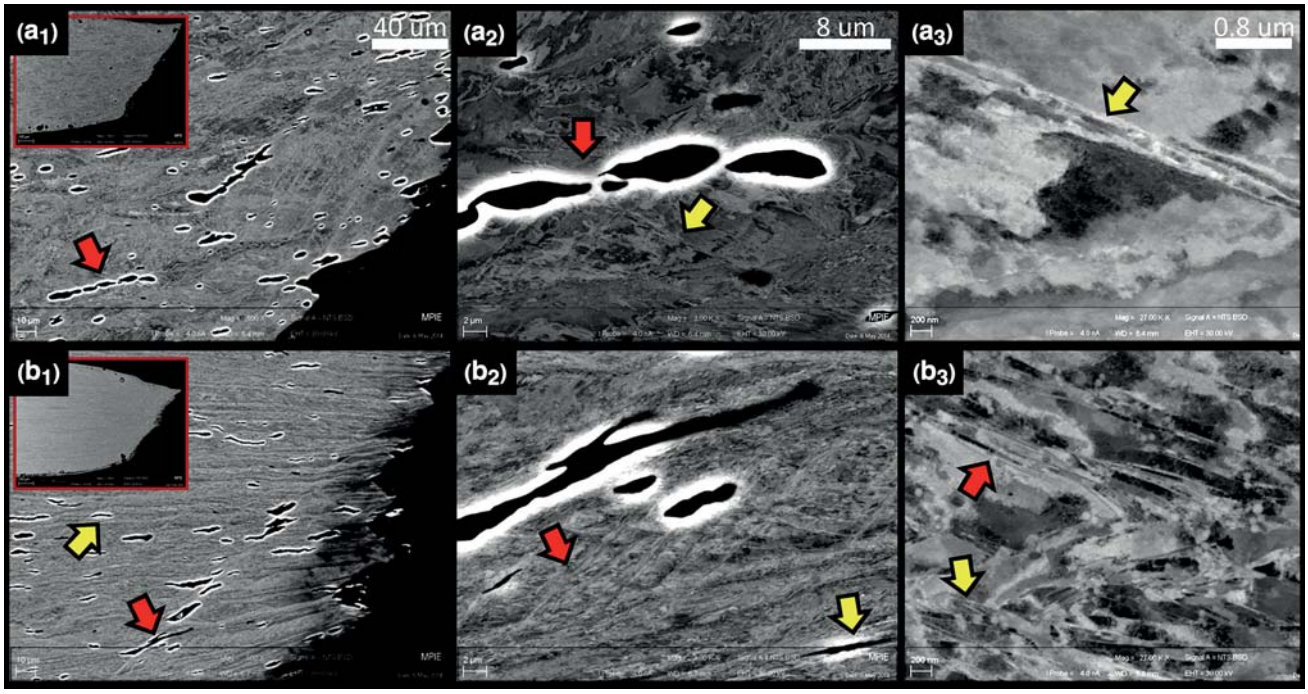

Fig. 8. Microstructural damage mechanisms in (a) $Fe_{40}Mn_{27}Ni_{26}Co_5Cr_2$ and (b) $Fe_{37}Mn_{45}Co_9Cr_9$ alloys.

classified as HEAs, only one of the three criteria proposed in the literature can predict the single-phase SS formation in these alloys correctly (see criteria B in Table I). However, all three criteria (including criteria B) predict the four-component equiatomic $Co_{25}Cr_{25}Fe_{25}Mn_{25}$ alloy to develop a single-phase SS, which is not accurate as shown in Fig. 2. These alloy trend observations show that not the CE alone but rather the free energy determines the stability of an SS.

The analysis of deformation mechanisms presented in Figs. 5, 6, 7, and 8 reveals a classic austenitic dislocation slip-based plasticity, except at very high (local) strain levels. These observations

Table I. Comparison of different SS criteria for the investigated alloys

	δ (%)	ΔH_{mix} (J/K * mol)	$\Delta S_{conf.}$ (J/K * mol)	Ω	Criteria A[2]	Criteria B[3]	Criteria C[4,5]	Single phase
$Co_{20}Cr_{20}Fe_{20}Mn_{20}Ni_{20}$	4.19	–4.16	13.38	5.76	Pass	Pass	Pass	Yes
$Fe_{40}Mn_{27}Ni_{26}Co_5Cr_2$	4.58	–3.56	10.84	5.21	Pass	Pass	Fail	Yes
$Fe_{37}Mn_{45}Co_9Cr_9$	4.95	–0.95	9.65	17.29	Fail	Pass	Fail	Yes
$Co_{25}Cr_{25}Fe_{25}Mn_{25}$	4.53	–2.25	11.53	9.25	Pass	Pass	Pass	No

are supported by the similarity of the stress–strain response shown in Fig. 4 to those of fully austenitic Fe-Mn steels (see, e.g., Fig. 4 in Ref. 29). Given the absence of other dislocation barriers and the "easy" possibility of transition from planar to wavy slip, the main strain-hardening contributions are observed to originate from pileups of dislocations at grain boundaries at low deformation levels (Fig. 7a_1, b_1) as well as from the reduced dislocation mean-free path because of the fast-developing in-grain dislocation substructure (Fig. 7a_4, b_2) at higher deformation levels.

From the perspective of mechanical properties, although it is rather contrary to what is expected in massively SS strengthened alloys (e.g., other HEA), the excellent tensile ductility and low strength combinations reported for this alloy system correlate well with the presented single fcc phase microstructures and the deformation mechanisms. A wider perspective can be gained by considering the achieved properties with respect to those of Fe-Mn binary alloys (Fig. 4b). Although strong SS strengthening contributions exist in the current alloys compared with fully austenitic Fe-Mn binary systems (with >28 wt.% Mn, see Fig. 4b), extending the comparison to other (multiphase) Fe-Mn binary systems (Fig. 4b), or to currently widely investigated medium or high Mn steels with significantly less alloying,[31,32] the room-temperature property achievements appear limited for all CoCrFeMnNi system alloys considered here. The fcc microstructure does exhibit excellent thermal stability;[10,12] yet, the loss of both ductility and strength limits high-temperature applications of this system. Promising cryogenic behavior,[12] and the strong crack propagation resistance observed here in the severely cold-worked state enabling excellent toughness, both underline the significance of mechanical nanotwinning. Thus, given the first indications of wide phase stability observed in this article for different compositions, compositional changes can be considered in future work to decrease the stacking fault energy and to introduce a mechanically induced twinning mechanism at room temperature. The unexpectedly strong Hall-Petch contribution[10,16] motivates further investigation of contributions from other (traditional) strengthening mechanisms as well.

CONCLUSION

The heavy alloying requirements and the relatively small gains in mechanical performance (even with respect to some binary Fe-Mn systems) limit the room- or high-temperature applications of the most successful HEA $Co_{20}Cr_{20}Fe_{20}Mn_{20}Ni_{20}$. The presented investigations reveal that the compositional requirements to stabilize the massive solid solution fcc phase in this alloy system are more relaxed what was originally proposed. Moreover, as expected from the similar deformation mechanisms observed (e.g., planar slip, nanotwinning, etc.), nonequiatomic HEA demonstrate mechanical performances comparable with those of the equiatomic alloy. Thus, well-controlled compositional variations can now be considered not only to decrease the processing and alloying costs but also to explore improved mechanical property combination, e.g., by the introduction of a mechanically induced twinning mechanism at room temperature.

ACKNOWLEDGEMENTS

The authors would like to gratefully acknowledge the financial support by the European Union via the ERC Advanced Grant "SMARTMET" and the contributions of Michael Kulse, Frank Schlüter, Frank Rütters, Michael Adamek, Jiali Zhang, and Motomichi Koyama.

REFERENCES

1. J.W. Yeh, S.K. Chen, S.J. Lin, J.-Y. Gan, T.-S. Chin, T.-T. Shun, C.-H. Tsau, and S.-Y. Chang, *Adv. Eng. Mater.* 6, 299 (2004).
2. Y. Zhang, Y.J. Zhou, J.P. Lin, G.L. Chen, and P.K. Liaw, *Adv. Eng. Mater.* 10, 534 (2008).
3. Y. Zhang, X. Yang, and P.K. Liaw, *JOM* 64, 830 (2012).
4. S. Guo, C. Ng, J. Lu, and C.T. Liu, *J. Appl. Phys.* 109, 103505 (2011).
5. S. Guo and C. Liu, *Prog. Nat. Sci. Mater. Int.* 21, 433 (2011).
6. B. Cantor, I.T.H. Chang, P. Knight, and A.J.B. Vincent, *Mater. Sci. Eng. A* 375, 213 (2004).
7. O.N. Senkov, G.B. Wilks, J.M. Scott, and D.B. Miracle, *Intermetallics* 19, 698 (2011).
8. O.N. Senkov, J.M. Scott, S.V. Senkova, D.B. Miracle, and C.F. Woodward, *J. Alloy. Compd.* 2011, 6043 (2011).
9. F. Otto, Y. Yang, H. Bei, and E.P. George, *Acta Mater.* 61, 2628 (2013).
10. M.J. Yao, K.G. Pradeep, C.C. Tasan, and D. Raabe, *Scripta Mater.* 72, 5 (2014).
11. K.G. Pradeep, N. Wanderka, P. Choi, J. Banhart, B.S. Murty, and D. Raabe, *Acta Mater.* 61, 4696 (2013).

12. F. Otto, A. Dlouhy, C. Somsen, H. Bei, G. Eggeler, and E.P. George, *Acta Mater.* 61, 5743 (2013).
13. Z. Wu, H. Bei, F. Otto, G.M. Pharr, and E.P. George, *Intermetallics* 46, 131 (2014).
14. P.P. Bhattacharjee, G.D. Sathiaraj, M. Zaid, J.R. Gatti, C. Lee, C.-W. Tsai, and J.-W. Yeh, *J. Alloy. Compd.* 587, 544 (2014).
15. K.-Y. Tsai, M.-H. Tsai, and J.-W. Yeh, *Acta Mater.* 61, 4887 (2013).
16. W.H. Liu, Y. Wu, J.Y. He, T.G. Nieh, and Z.P. Lu, *Scripta Mater.* 68, 526 (2013).
17. A. Gali and E.P. George, *Intermetallics* 39, 74 (2013).
18. C. Zhu, Z.P. Lu, and T.G. Nieh, *Acta Mater.* 61, 2993 (2013).
19. G.A. Salishchev, M.A. Tikhonovsky, D.G. Shaysultanov, N.D. Stepanov, A.V. Kuznetsov, I.V. Kolodiy, A.S. Tortika, and O.N. Senkov, *J. Alloy. Compd.* 591, 11 (2014).
20. M.S. Rashid, *Ann. Rev. Mater. Sci.* 11, 245 (1981).
21. S. Sadagopan and D. Urban, *AISI/DOE Technology Roadmap Program* (Oak Ridge, TN: Office of Scientific and Technical Information, 2003).
22. M. Calcagnotto, Y. Adachi, D. Ponge, and D. Raabe, *Acta Mater.* 59, 658 (2011).
23. T. Dursun and C. Soutis, *Mater. Des.* 56, 862 (2014).
24. H. Springer and D. Raabe, *Acta Mater.* 60, 4950 (2012).
25. I. Gutierrez-Urrutia, S. Zaefferer, and D. Raabe, *Scripta Mater.* 61, 737 (2009).
26. S. Mandal, K.G. Pradeep, S. Zaefferer, and D. Raabe, *Scripta Mater.* 81, 16 (2014).
27. C.C. Tasan, J.P.M. Hoefnagels, and M.G.D. Geers, *Scripta Mater.* 62, 835 (2010).
28. A. Holden, J.D. Bolton, and E.R. Petty, *J. Iron Steel* I, 721 (1971).
29. Y. Tomota, M. Strum, and J.W. Morris Jr., *Metall. Trans. A* 17A, 537 (1986).
30. A.L. Schaeffler, *Metal Progr.* 56, 680 (1949).
31. U. Brüx, G. Frommeyer, O. Grässel, L.W. Meyer, and A. Weise, *Steel Res.* 73, 294 (2002).
32. H. Ding, H. Ding, D. Song, Z. Tang, and P. Yang, *Mater. Sci. Eng. A* 528, 868 (2011).